aerospace

MDPI

Article

Analysis of the Effect of the Leading-Edge Vortex Structure on Unsteady Secondary Flow at the Endwall of a High-Lift Low-Pressure Turbine

Shuang Sun [1], Jinhui Kang [1], Zhijun Lei [2,*], Zhen Huang [1], Haixv Si [1] and Xiaolong Wan [1]

[1] College of Aeronautical Engineering, Civil Aviation University of China, 2898 Jinbei Road, Dongli District, Tianjin 300300, China
[2] Institute of Engineering Thermophysics, Chinese Academy of Sciences, Beijing 100045, China
* Correspondence: leizhijun@iet.cn

Abstract: The horseshoe vortex system at the leading edge of a low-pressure turbine (LPT) has unsteady flow characteristics, and the flow field in the downstream cascade channel also has unsteady characteristics. In this study, CFD simulations are performed with the help of commercial software CFX, and experimental checks are performed using a fan-shaped cascade test bench to investigate the flow characteristics of the endwall of the PACKB blade type of a high-lift LPT under the same incoming Reynolds number and two incoming boundary layer thickness conditions. The obtained results show that there are different flow alteration characteristics and alteration frequencies of the horseshoe vortex system, among which the vortex system with a thicker boundary layer is larger in size and less spaced from each other, which is more likely to induce the fusion of vortex systems. The centrifugal instability causes the instability of the horseshoe vortex system, and the instability frequency is inversely proportional to the thickness of the boundary layer. With two inlet boundary layers, the instability frequencies of the vortex system are 125 Hz and 175 Hz, respectively, and the ratio of the frequency to the thickness of the boundary layer is reciprocal to each other. The stimulation effect of the unstable horseshoe vortex system on the downstream secondary flow intensity is greater than that of the steady state. The thin boundary layer case generates a greater unsteady loss in the cascade channel than the thick boundary layer case due to the poor stability of the vortex system.

Keywords: high-lift low-pressure turbine; flow instability; leading edge vortex structure; secondary flow

Citation: Sun, S.; Kang, J.; Lei, Z.; Huang, Z.; Si, H.; Wan, X. Analysis of the Effect of the Leading-Edge Vortex Structure on Unsteady Secondary Flow at the Endwall of a High-Lift Low-Pressure Turbine. *Aerospace* **2023**, *10*, 237. https://doi.org/10.3390/aerospace10030237

Academic Editor: Pietro Catalano

Received: 20 January 2023
Revised: 24 February 2023
Accepted: 25 February 2023
Published: 28 February 2023

1. Introduction

In the LPT endwall flow, the horseshoe vortex develops from the leading edge downstream. This makes the secondary vortex system at the channel endwall more complicated and has a direct effect on the endwall flow losses, which can be as much as one-third or more of the total secondary flow losses [1–6]. Dossena et al. [7] and Weiss et al. [8] pointed out that the increase in blade loading will enhance the LPT endwall secondary flow and increase the endwall flow losses. For the turbine endwall flow structure, Langston et al. [9] earlier proposed a turbine endwall secondary flow model, which gives the development of the boundary layer into a horseshoe vortex (HSV) and its evolution into a passage vortex. Hodson et al. [10] also conducted experimental analysis on the flow structure in the endwall region of low-pressure turbines, and found that the flow characteristics in the endwall region of turbines are mainly reflected in the evolution mode of passage vortices and horseshoe vortices, the formation of corner vortices, the interaction between trailing edge shedding vortices and suction surface separation bubbles. Zoric et al. [11,12] experimentally compared the endwall flow of three loaded LPTs and found that the passage vortex and trailing shedding vortex were significantly enhanced in the front-loaded PACKD-F blade type due to the intense acceleration in the front half of the cascade channel, which in turn increased the secondary flow losses. Diego Torre et al. [13] used a nonaxisymmetric

contoured endwall to control the flow losses in the LPT endwall. The unique endwall shape increases the vorticity of the HSV suction leg and decreases the vorticity of the pressure leg. This reduces the interaction between the pressure leg and the pressure surface separation and suppresses the intensity of their development into the passage vortex. In addition, the convective heat transfer near the junction of the endwall and the HSV cascade is 200% higher than that in the upstream boundary layer [14]. Thus, it is particularly important to investigate the unsteady characteristics of the HSV system.

Among them, Devenport and Simpson [15] studied the structure of the HSV near the leading edge of a wing at Re = 115,000 and found by their analysis that the HSV is characterized by low-frequency oscillations, generating bimodal probability density functions (pdfs) of horizontal and vertical velocities in the plane of symmetry. It was also demonstrated that the HSV has a periodic alternation between the back-flow and zero-flow modes, with irregular and relatively long time intervals (low frequency) for the switching between the modes. Based on the flow field measured by PIV, Praisner and Smith [14] proposed that the switching between the back-flow and zero-flow modes is determined by the interaction between the boundary layer of the HSV vortex system and the near-wall reflux. Vortex-resolved numerical simulations by Paik et al. [16] and Escauriaza [17] showed that the transition from the back-flow mode to the zero-flow mode is triggered by hairpin vortices generated by the interaction of the HSV with the wall. Apsilidis et al. [18] subsequently suggested that a third intermediate mode exists for a significant portion of time. In the intermediate mode, the wall jet neither penetrates the upstream vortex system to form a complete return flow nor produces a vertical upward jet but only diffuses near the boundary layer. Chenqigang [19] studied the dynamics of the HSV vortex system around a cylinder with Re = 8600–13,900 and argued for the existence of the intermediate mode by analyzing the velocity field. The nonperiodic interaction between the fundamental flow states generates high turbulent stresses in the HSV region, and the interaction of turbulent stresses and vortex system structure is also observed among other geometrical configurations [20–22].

Escauriaza et al. [17] showed that the time-averaged HSV vortex system consists of two clockwise rotating vortices (HV1) and (HV2), a counterclockwise rotating corner vortex (CV) located downstream of HV1, and a third vortex (HV3) between HV1 and HV2. In response to this finding, Apsilidis et al. [18] suggested the possibility that vortex HV2 is not a coherent flow structure but a time-averaged series of various small vortices. Escauriaza [17] and Dargahi [23] observed that the structure of their vortex system consists mainly of two main vortices instead of one. Simpson [24] pointed out that the HSV vortex system has the characteristics of intermittent wall fluid ejection and disorderly movement of the main vortex, similar to the eruption event. HSV vortex systems exhibit cyclic and periodic dynamics of vortex structure regeneration and jet eruption vortex destruction. Agui and Andreopoulos [25] demonstrated that the typical feature of HSV vortex systems is a mushroom-like vortex structure generated by a continuous eruption of near-wall fluids between the wall and the main HSV, which interacts with the main horseshoe vortex. Similar observations exist in the laminar flow state [26,27], where counterrotating vortices emerging from the wall interact with the HSV, leading to HSV disintegration and periodic regeneration. Escauriaza [23] pointed out that the interaction between the back-flow mode and zero-flow mode is the result of the development of small-scale hairpin vortices and that the change in flow curvature near the wall triggers the centrifugal instability of the HSV. During the vortex outburst at the near-wall surface where the HSV vortex system is disrupted, hairpin vortices are formed there, which in turn trigger the zero-flow mode of the near-wall reflux vertical jet.

However, the structure of the horseshoe vortex is very complex, and the discussion of the flow topology of the vortex system is incomplete. The traditional RANS-based calculation method has limitations [15] because it cannot capture the instability of the HSV system. Su [28] used a DDES simulation method to study the periodic variation of the vortex system at the leading edge of a high-lift turbine cascade at higher Mach numbers

and its development within the cascade channel. This study revealed that the overall losses would be greatly underestimated if the nonconstant effects within the grille channel were not considered. The effect of the Reynolds number on the HSV vortex system has been studied by numerous authors [15,21,23]. The boundary layer thickness characteristics will have a significant impact on the HSV dynamics and thus on the development of the channel vortex. However, relatively little research has been conducted on the downstream flow of the HSV channel.

In this study, the typical LPT Reynolds number incoming flow of Re_{in} = 100,000 is selected as the reference condition. The boundary layer thickness of this condition is taken as the reference. The boundary layer thickness is increased to 1.4 times the reference condition by extending the hub length of the leading edge of the blade. After the preliminary analysis, it was found that a small difference in the incoming boundary layer thickness would not cause a change in the leading edge vortex system, and 1.4 times the boundary layer thickness could form a large difference in the leading edge vortex system.

The novelty of this paper is that the traditional RANS method cannot calculate the instability of the vortex system. Therefore, in this paper, considering the instability of HSV, the LES method and POD theory are adopted to analyze the dynamic characteristics of the HSV vortex system under different boundary layer thicknesses in detail. Additionally, the influence of the vortex system on the flow characteristics of the endwall is studied. The influence of turbulent pulsation component on unsteady loss in the cascade channel is analyzed and the influence of boundary layer thickness on the flow loss mechanism of the cascade endwall is obtained. Through this paper, we can gain a deeper understanding of the vortex system in low-pressure turbines. This paper provides a suggestion for the subsequent design of low-pressure turbines, i.e., proper consideration should be given to the loss caused by the instability of the vortex system.

2. Numerical Method and Experimental Verification

2.1. Numerical Methods

In recent years, LES has been widely used in low-pressure turbine endwall flow research [29,30]. In this study, numerical simulations were performed using the commercial CFD software ANSYS CFX 15.0. The LES model combined with the Smagorinsky subgrid model was used to predict the spatial distribution of turbulent kinetic energy, vortex structure, and HSV flow dynamics phenomena [26,27]. In the calculation of LES in this paper, the governing equation adopted is the incompressible N-S equation after filtering:

$$\frac{\partial \bar{u_i}}{\partial t} + \frac{\partial \bar{u_i}\bar{u_j}}{\partial x_j} = -\frac{1}{\rho}\frac{\partial \bar{p}}{\partial x_i} - \frac{\partial \tau_{ij}}{\partial x_j} + \frac{\partial}{\partial x_j}(\nu \frac{\partial \bar{u_i}}{\partial x_j}) \tag{1}$$

$$\frac{\partial \bar{u_i}}{\partial x_i} = 0 \tag{2}$$

where τ_{ij} is subgrid-scale stress, defined as:

$$\tau_{ij} = \overline{u_i u_j} - \overline{u_i u_i} \tag{3}$$

In the present simulation, to avoid the disadvantages of the Smagorinsky model, the Van-Driest wall dumping function was used, according to the studies by Tomikawa [31]. These settings could accurately simulate the unsteady flow of the LPT at low Reynolds numbers [32]. Application of Smagorinsky model-based LES to the analysis of the transitional boundary layer may be open to dispute. However, several examples have proved that reasonable results can be obtained for computational grid systems with high quality and a large number of grid points [32,33]. Although this method cannot completely eliminate the disadvantages of the Smagorinsky model, it can still capture the configuration changes of leading-edge vortex systems. Therefore, these results can be interpreted as possible, stable solutions.

The studied cascade type is PACKB, and the geometric and aerodynamic parameters of the leaf grille are shown in Table 1. In Re_{in}, where characteristic length D is defined as axial chord length at different blade heights, V is the inlet velocity and μ is the viscosity.

Table 1. Geometric and aerodynamic parameters of the cascade.

Parameters	Values
Chord length, C	145 mm
Axial chord length, Cx	139 mm
Blade height, h	300 mm
Inlet angle	35°
Exit angle	60°
Load coefficient, Zw	1.08
Inlet velocity	12 m/s
Free stream turbulence intensity (FSTI)	5%
$Re_{in} = \rho VD/\mu$	100,000

The computational domain contains a cascade channel, and the geometric model of the calculation is shown in Figure 1. The blade surface and endwall are adiabatic no-slip walls, and the thickness of the boundary layer at the leading edge of the cascade is controlled by adjusting the length of the no-slip wall surface at the inlet from the leading edge of the cascade. Constant velocity boundary conditions are adopted at the cascade inlet, the pressure boundary condition is adopted at the outlet, and the value is set as standard atmosphere pressure.

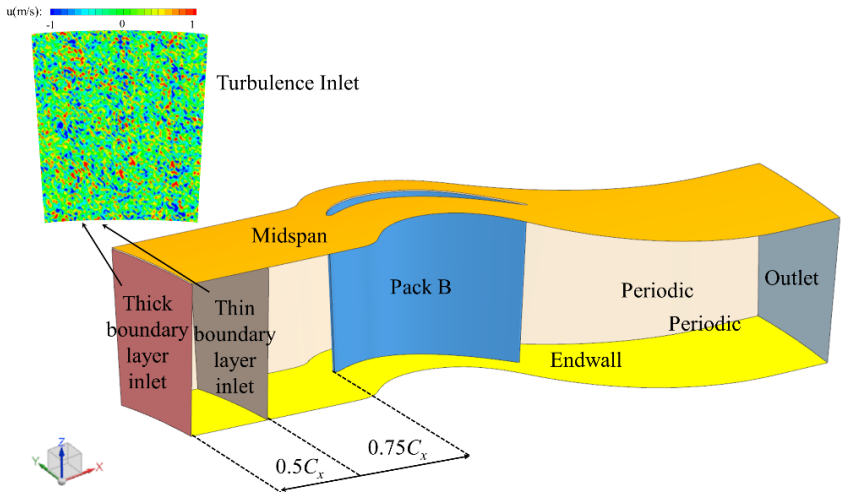

Figure 1. Computing domain model settings.

The inlet external turbulence will affect the coherent structure in the flow field. To capture the coherent structure of horseshoe vortices accurately, external turbulence synthesis must be carried out. By synthesizing external turbulence, the coherent structure can be captured successfully by the Smagorinsky subgrid model [34]. The inlet turbulence intensity is generated by the SNGR (Stochastic Noise Generation and Radiation) method used in the previous work [35]. The SNGR method has been widely used to predict low-pressure turbine flow at low Reynolds numbers. According to the SNGR method, a turbulent velocity can be generated. The turbulence intensity and integral turbulence length values in the numerical simulation are derived from experimental measurements and set in the SNGR method. To save computational resources, only the half-blade height is calculated, and the half-blade height surface is set as the free slip wall boundary condition.

The topology of the cascade channel is shown in Figure 2, and the computational domain is divided into an "HOH" − type mesh topology; an "O" grid is used around the

blade wall, and an "H" grid is used at the inlet and outlet of the cascade. The trailing edge of the blade is $1.5C_x$ away from the outlet of the computational domain, which is used to reduce the numerical reflection at the outlet position.

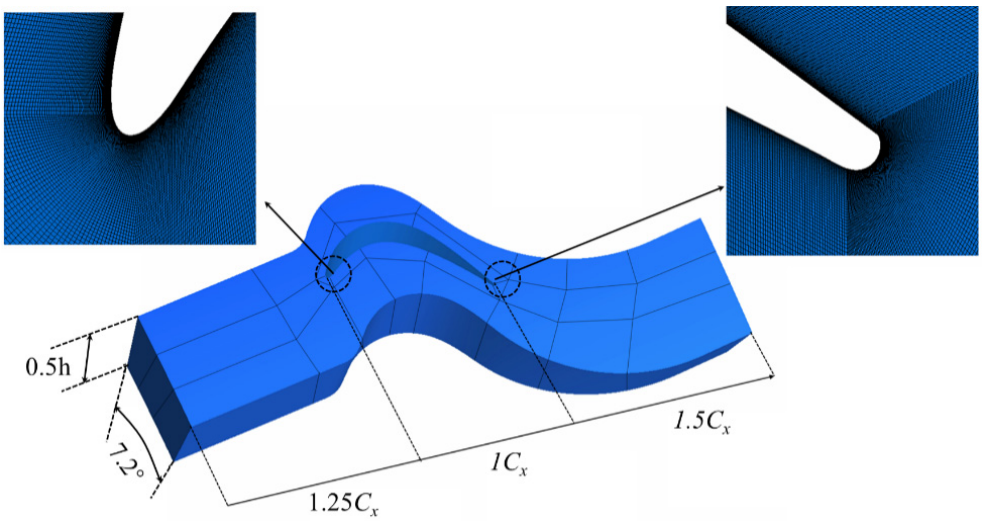

Figure 2. Cascade computing region.

Figure 3 shows the verification results of grid independence calculated by different grid node numbers. When the number of grid nodes is below 12 million, the average loss calculation deviation of the outlet surface is large. The encryption strategy of the grid is not simply to increase the number of grid nodes, because this encryption strategy will result in ineffective encryption of the grid whose location is not affected by the secondary flow. Considering the simulation stability and cost, 15 million is finally selected as the grid number. The average export loss Y_P is defined as:

$$Y_P = (P_{t1} - P_{t2})/(P_{t1} - P_1) \tag{4}$$

where P_{t1} represents the total pressure at the turbine cascade inlet, P_{t2} represents the total pressure at the turbine outlet, and P_1 represents the static pressure at the inlet.

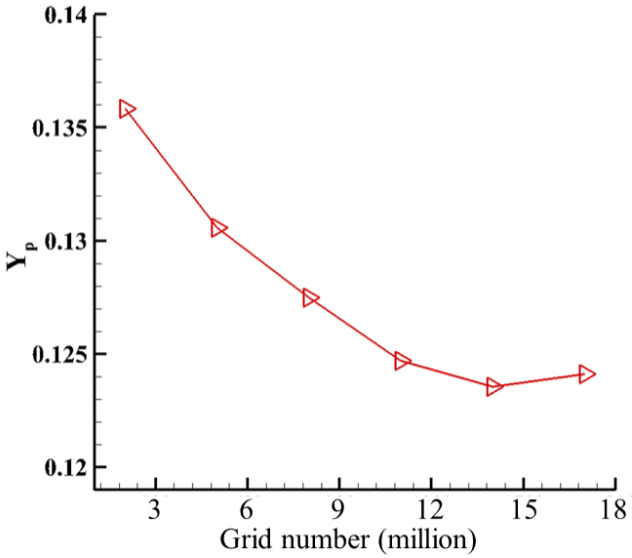

Figure 3. Grid independence analysis.

The computational domain consists of 15 million grid cells with a maximum thickness of 0.0025 mm from the first layer of the Endwall grid in the blade normal direction, guar-

anteeing y+ < 1 and Δx+ = 20 and Δz+ = 12 (x is the flow direction, and z is the spanwise direction). The SST turbulence model combined with the $\gamma-\mathrm{Re}\theta$ transition model is first used to advance the calculation method by 1000 steps, and the convergence of the SST turbulence model is taken as the initial field of unsteady calculation results. The time step is then set to 2×10^{-5}, which is smaller than the estimated Kolmogorov time scale, which ensures that the maximum Courant–Friedrichs–Lewy number is less than 1. And the movement of the particle can be guaranteed to be less than the minimum mesh size, which gives sufficient accuracy to the particle tracking in the following [26].

The second-order central difference scheme is adopted in space scheme, and the second-order backward difference scheme is adopted in time scheme.. The pressure-velocity coupling is high resolution and the spatial discretization used for gradients, pressure, and momentum is central difference. The unsteady flow field is stabilized by advancing 2000 steps with approximately four leading-edge vortex system cycles. After 5000 steps, unsteady statistics of approximately 10 HSV vortex system periods were performed. To meet the iterative convergence criterion: the residuals of velocity and pressure in three directions are less than 0.0001, and each time step is iterated 20 times. The calculations were simulated on a computer with an EPYC7742 CPU and 64G 3200−MHz memory.

For the LES simulation, the majority of the turbulent kinetic energy should be resolved instead of being modeled. Pope [36] suggests that the proportion of turbulent kinetic energy solved should be greater than 80%, which follows the following criteria:

$$\phi = \frac{0.5\overline{u'_i u'_i}}{E_{sgs} + 0.5\overline{u'_i u'_i}} > 0.8 \tag{5}$$

where E_{sgs} is the modeled turbulent kinetic energy. This parameter can be solved by the method proposed by Deardorff [37]. In this paper, the average value of ϕ in the calculation domain is about 0.9, which means that only 10% of the turbulent kinetic energy is modeled by the LES scheme.

2.2. Experimental Settings

The endwall flow experiments in this study were performed in the low-speed fan-shaped turbine cascade laboratory of the Civil Aviation University of China. The structure of the cascade experimental bench is shown in Figure 4. The experimental bench is mainly composed of five parts: a centrifugal fan (air source), honeycomb section, rectification section, fan shrinkage section, and fan experimental section. The maximum working power of the fan can reach 55 kW, and the maximum air volume of the air source is 40,000 m^3/h. The experimental section is mainly composed of an inlet guide vane and a static vane. The geometric scale of the fan-shaped cascade is consistent with that in Table 1, and the cascade consists of twelve blades. A series of static pressure holes are arranged at 5% and 40% of the blade height for static pressure data acquisition on the suction surface. Adjusting plates are arranged on the left and right sides of the cascade passage to ensure the uniformity of the inlet and periodicity of the outlet of the cascade passage, respectively. After adjustment, it can be ensured that the flow angle fluctuation at the inlet of the three blade passages is less than 0.5° and the static pressure fluctuation at the inlet of the blade is less than 1% of the dynamic pressure at the outlet. At the same time, the boundary layer thickness at the leading edge of the cascade can be changed by changing the casing and hub with different flow lengths.

As shown in Figure 5, the DSA 3217 pressure transducer from Scanivalve was used in conjunction with wall hydrostatic bores and a seven-hole probe to test the blade loads. Boundary layer and turbulence intensity tests were performed using a Dantec 55P11 monofilament hot wire with Dantec StreamLine Pro.

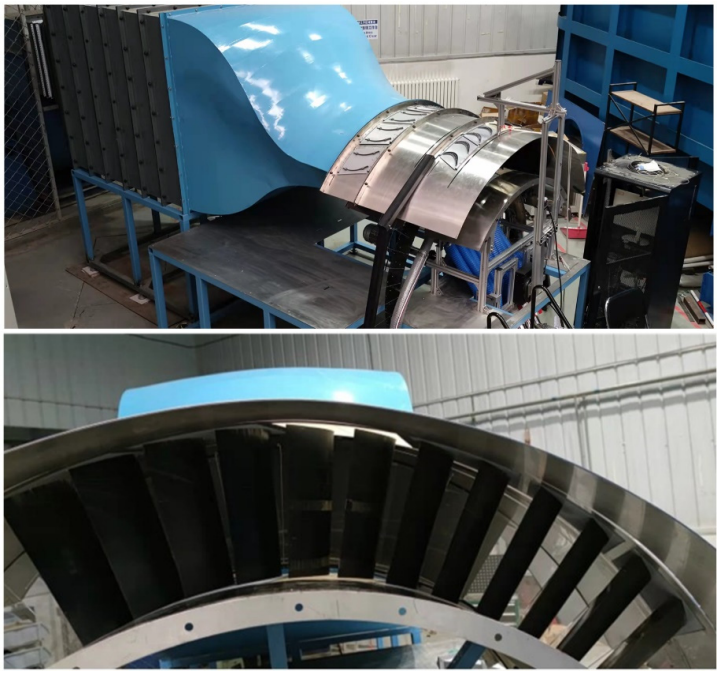

Figure 4. Fan-shaped cascade test bench setup.

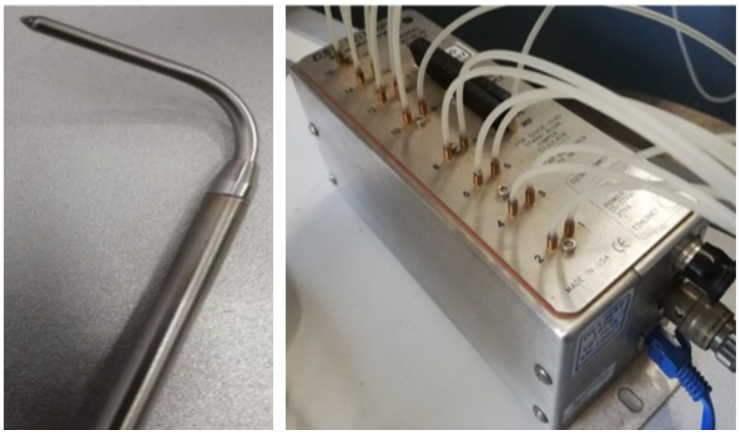

Figure 5. Experimental measuring device setup.

The FSTI of 5% was generated by square-mesh arrays with round rods. The correlations of Roach [38] were used to design the turbulence grids to achieve higher freestream turbulence intensity. The diameter of the rod used for the grid was d = 14 mm, and the grids were arranged 1.4 m upstream of the cascade to produce a steady FSTI. The FSTI and the turbulence integral length compared with Roach's correlation are shown in Figure 6. The FSTI was measured by a 55P11 hot-wire probe, and the turbulence integral length was obtained, referring to Hinze [39], based on the measurement results. Then, the turbulence intensity and turbulence integral length data obtained from the experiment were statistically analyzed. Consequently, the SNGR method is used to generate inlet turbulence that is consistent with the experimental turbulence intensity and turbulence integral length data.

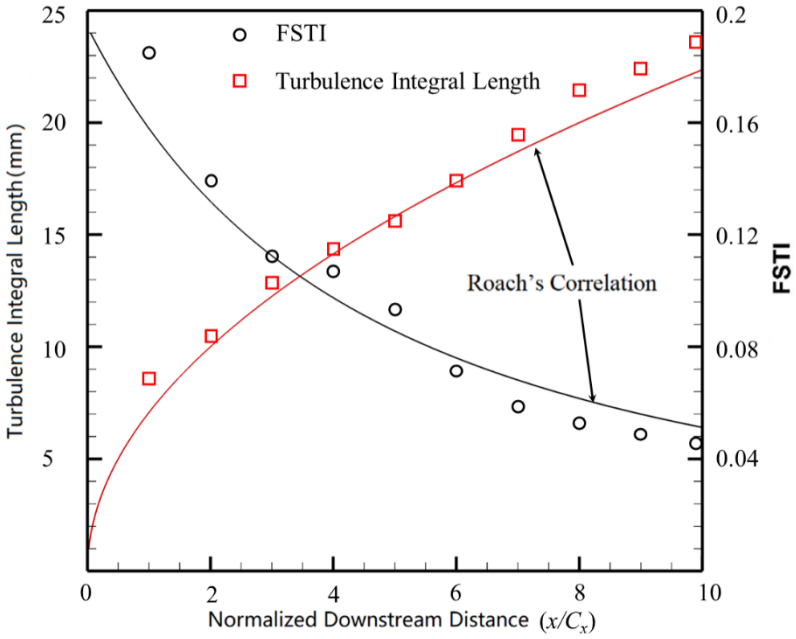

Figure 6. FSTI and turbulence integral length scale.

2.3. Uncertainty Analysis

The uncertainty of the experimental dataset was estimated according to the measurement uncertainty expression guide [40]. The mathematical expression [41] of experimental uncertainty was used:

$$\delta F = \pm \sqrt{\sum_{i=1}^{N} \left(\frac{\partial F}{\partial f_n} \partial f_n\right)^2} \tag{6}$$

where F is the total uncertainty and f is the independent uncertainty variable. The full-scale accuracy of the Scanivalve DSA 3217 was 0.12%, with approximate uncertainties of 1.7% and 3.5% for the inlet velocity and static pressure, respectively. In addition, the uncertainty in the hot-wire probe measurements was approximately 2%, mainly due to calibration errors.

2.4. Numerical Verification

To verify the accuracy and authenticity of the LES calculation method, Figure 7 shows the blade load distribution after averaging the results of the LES calculation at 5% and 40% blade height for thin boundary layer conditions, with the surface static pressure coefficient defined as [6,34]:

$$C_p = \frac{P_{t1} - P_{local}}{\rho U^2{}_{out}/2} \tag{7}$$

where P_{t1} is the total pressure of the incoming flow, P_{local} is the local static pressure, and $\rho U^2{}_{out}/2$ is the outlet dynamic pressure. In Figure 7, by comparing the numerical values with the experimental results, it can be seen that the position of the pressure platform and the peak velocity point of the two are in good agreement, and the numerical results can better reflect the flow environment of the experimental blade.

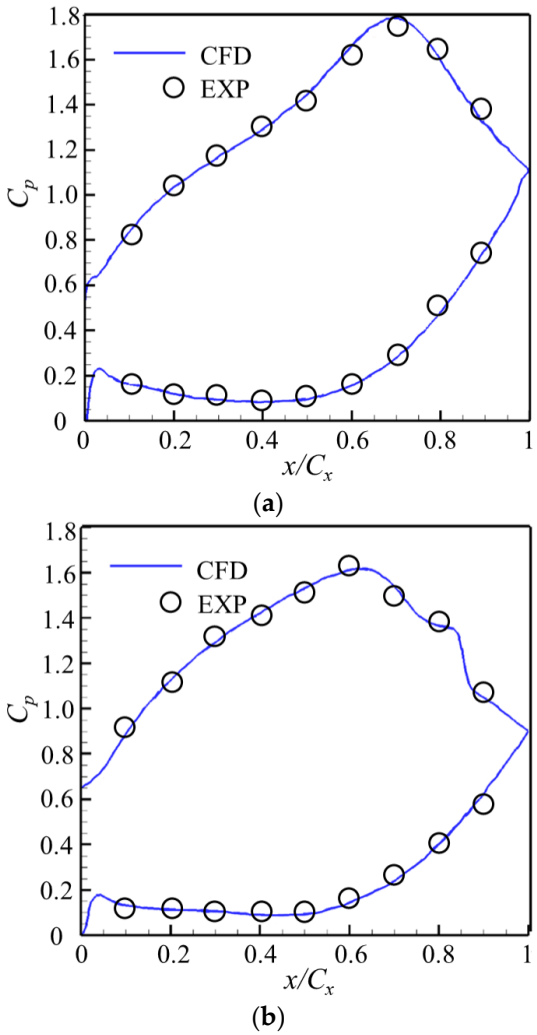

Figure 7. Distribution of the static pressure coefficient on the blade surface at different blade heights. (**a**) 5% blade hight (**b**) 40% blade hight.

3. Discussion of Results

3.1. Time-Averaged Flow Field Analysis

Figure 8 shows the cascade profile, Plane A observation plane, and the monitoring points used in the following sections, in which parameters such as chord length, axial chord length, and grid distance are indicated. In the figure, Plane A is an XZ plane whose range of flow direction length and radial height is larger than the existing range of the leading-edge vortex system, so this plane is selected for research.

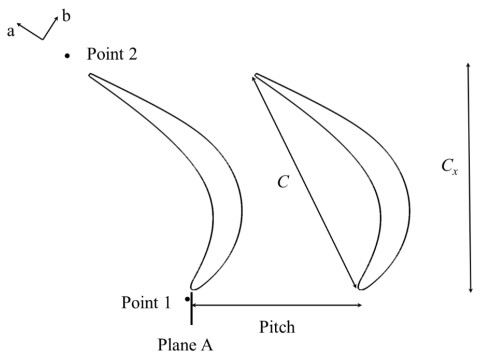

Figure 8. The cascade profile, Plane A observation plane, and the monitoring points are used in the following.

The time-averaged flow field analysis of the LES results at the location of Plane A in Figure 8 was selected, the endwall was colored using the time-averaged wall shear, and the results are shown in Figure 9. Since the thick boundary layer vortex system is more stable, the two vortices with close dimensions can be clearly distinguished by the time-averaged flow lines in Figure 9a. In Figure 9b, the vortex system is located closer to the leading edge of the blade in the flow direction, and only a larger vortex nucleus can be seen, which is close to the results of Baker et al. [42]. In Figure 9, both working conditions have clear positive and negative circular vorticity areas within the time-averaged flow field at the leading edge of the blade, and the positive vorticity area is approximately the same as the leading edge vortex system in the height range, while the negative vortex is concentrated at the bottom of the vortex system near the wall area. The average value of the positive and negative vortices in Figure 9b is larger than that in Figure 9a. The high wall shear region of the endwall is highly coincident with the leading edge vortex system as well as the HSV path [42], which can characterize the horseshoe vortex strength and action range. Compared to Figure 9b, Figure 9a has a larger endwall high wall shear region than Figure 9b due to the larger range of the vortex system. Because the vortex system is more stable, the instability phenomenon occurs less frequently, resulting in a smaller average amplitude in the high wall shear region of the endwall for the Figure 9a case than for the Figure 9b case.

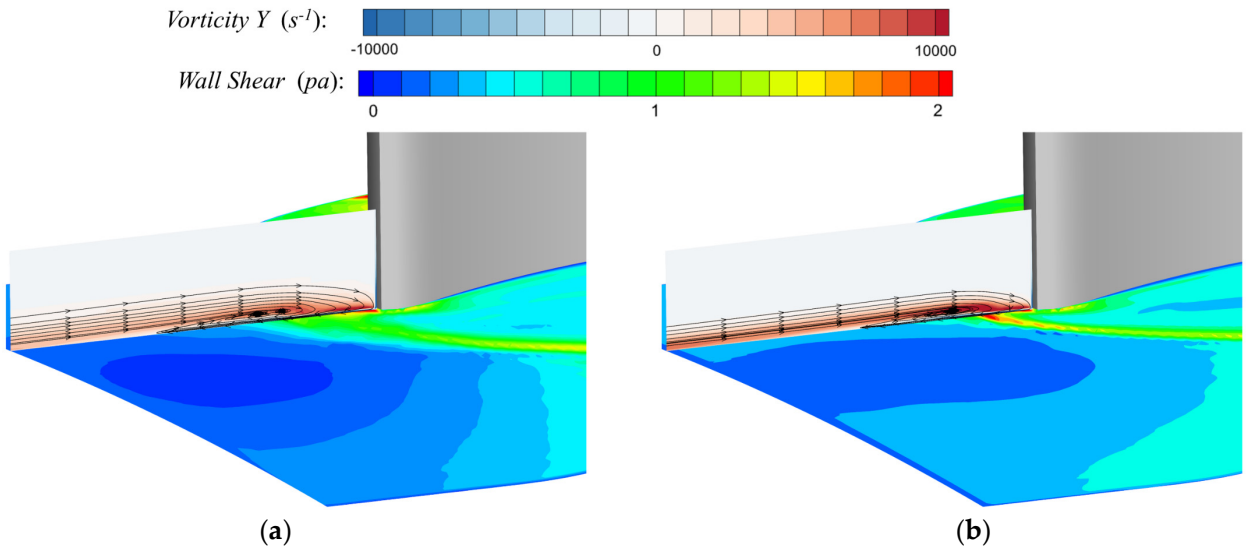

Figure 9. Plane A spatial distribution of mean streamlines and circumferential vorticity cloud. (**a**) Thick boundary layer case; (**b**) Thin boundary layer case.

The time-averaged turbulent kinetic energy of the LES results at the location of Plane A and the turbulence measured by the hot-wire anemometer are given in Figure 10, with the horizontal coordinate being the distance from the leading edge of the blade and the vertical coordinate being the height from the endwall. In Figure 10, the high turbulence region at Plane A is captured both experimentally and numerically. The higher turbulent kinetic energy region is approximately the same as the range of the leading edge horseshoe vortex system, and the values are in good agreement with the experiment. The high-turbulence energy region in Figure 10a is larger than that in Figure 10b in terms of both spanwise and flow coverage. The difference in the spanwise direction is due to the different thicknesses of the boundary layer, and the difference in the flow direction is due to the flow direction migration of the vortex system. Compared with the thick boundary layer condition, the high turbulent energy region in the thin boundary layer condition is more concentrated and close to the leading edge of the blade and has a higher turbulent energy amplitude. In Figure 10, the CFD result has little difference from the experimental measurement results, therefore, it can be considered that the CFD result is reliable.

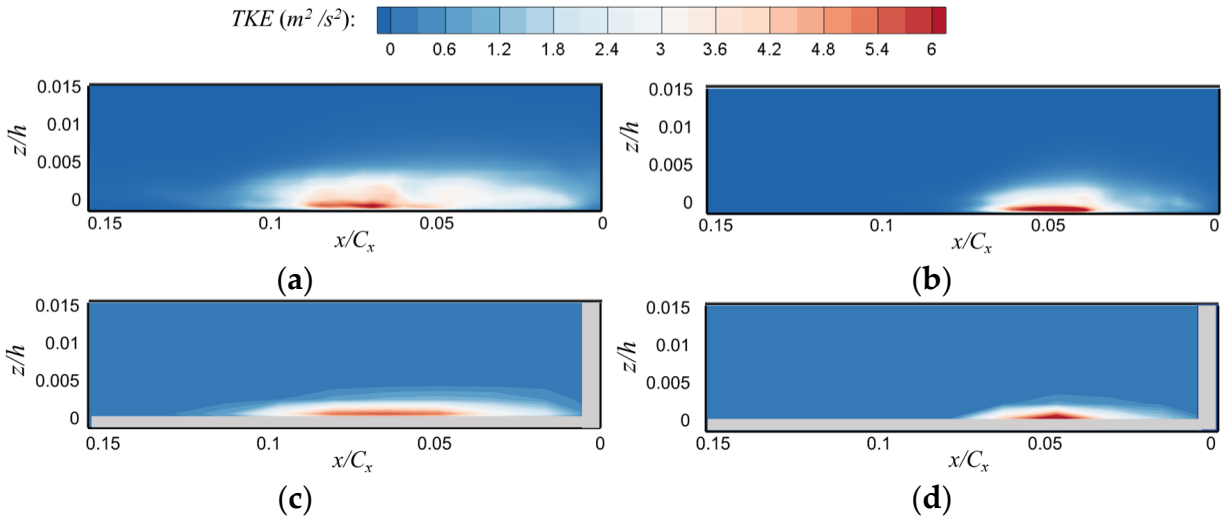

Figure 10. Turbulent kinetic energy distribution at Plane A3.2 Transient flow field analysis. (**a**) Thick boundary layer case (CFD); (**b**) Thin boundary layer case (CFD); (**c**) Thick boundary layer case (EXP); (**d**) Thin boundary layer case (EXP).

3.2. Transient Flow Field Analysis

3.2.1. HSV Vortex System Configuration Evolution

Figure 11 shows the typical flow patterns in the periodic motion of the HSV vortex system at the leading edge of the turbine cascade under the thick boundary layer working condition at the Plane A position. The contour image is the phase-locked average result of the transient flow field. At the initial moment in Figure 11a, there are two vortex systems, HV1 and HV2, in the flow field, the negative vorticity in the bottom backflow area is relatively stable, and the flow state corresponds to the backflow mode. At $t = 2/6T_1^*$, HV3 and its adjacent bottom secondary vortex appear in Figure 11b. At this time, the bottom backflow area is unstable and erupts, and jets erupt upward from the backflow near the wall but are unable to pass through the HSV vortex system to form a complete backflow. At the same time, the flow spacing between HV1 and HV2 is further than that of the backflow mode, and the vortex system is closer to the leading edge. This typical flow mode corresponds to the zero-flow mode. In Figure 11c, when the negative vorticity jet at the bottom caused by wall backflow is dissipated, the bottom backflow region tends to be stable again, and HV1 and HV2 begin to fuse. At this time, the distances between the three vortices of the HSV vortex system are relatively close, and the scale of the vortices begins to decrease compared with the zero flow mode in Figure 11b. In Figure 11d, HV1 is fused with HV2, and HV2 is close to HV3. In Figure 11e, the spacing between HV2 and HV3 is enlarged, and HV3 gradually moves upstream and increases in size. In Figure 11f, HV2 and HV3 are completely separated. At this time, the vortex system tends to be stable again, with the same back-flow mode as in Figure 11a and enters a new round of quasi-periodic cycles. At the same time, the time interval of the conversion of different flow modes is different, and the time interval of the same flow mode is also different. Therefore, this process is called the HSV vortex system quasi-periodic cycle.

Figure 12 shows the typical vortex system flow pattern in thin boundary layer conditions. Figure 12a is similar to Figure 12a, and both represent the backflow mode. Similar to Figure 11b, Figure 12b is a zero-flow mode and is also composed of three vortices. In Figure 12c, HV1 and HV2 are fused, and HV3 is far away from the abovementioned two vortices, which does not show the phenomenon of close spacing or mutual fusion in Figure 11c. The thin boundary layer condition directly enters the next quasi-periodic cycle without the separation process of HV2 and HV3.

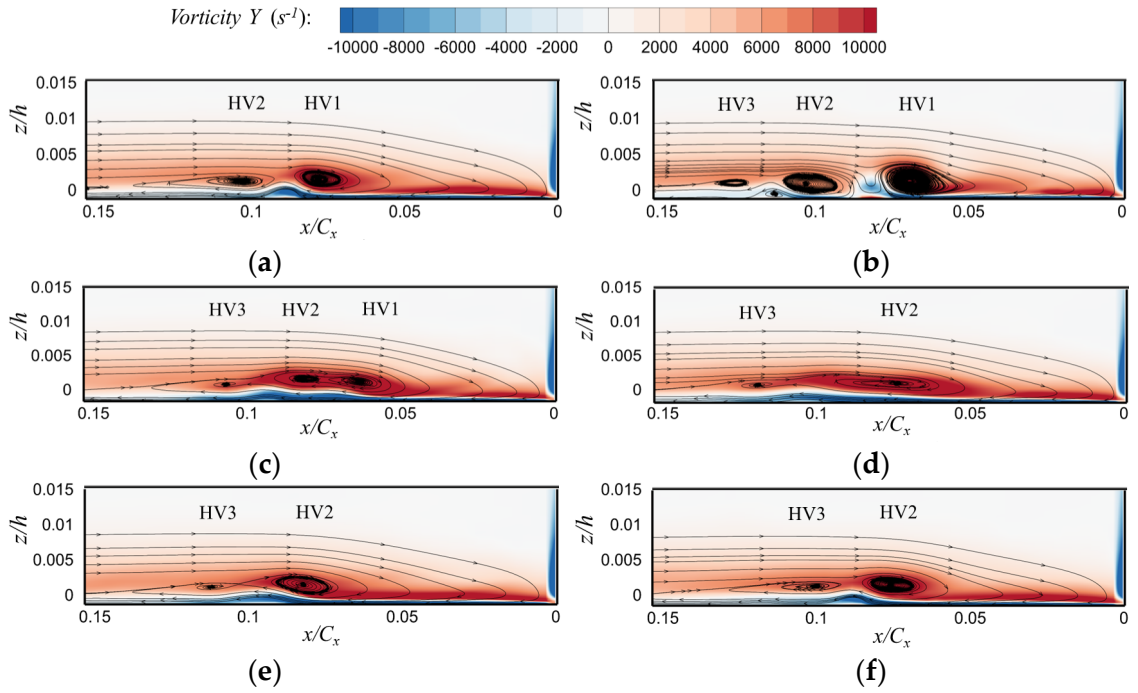

Figure 11. Typical flow pattern and circumferential vorticity contour of the HSV system with a thick boundary layer. (**a**) t = $1/6T_1^*$; (**b**) t = $2/6T_1^*$; (**c**) t = $3/6T_1^*$; (**d**) t = $4/6T_1^*$; (**e**) t = $5/6T_1^*$; (**f**) t = $6/6T_1^*$.

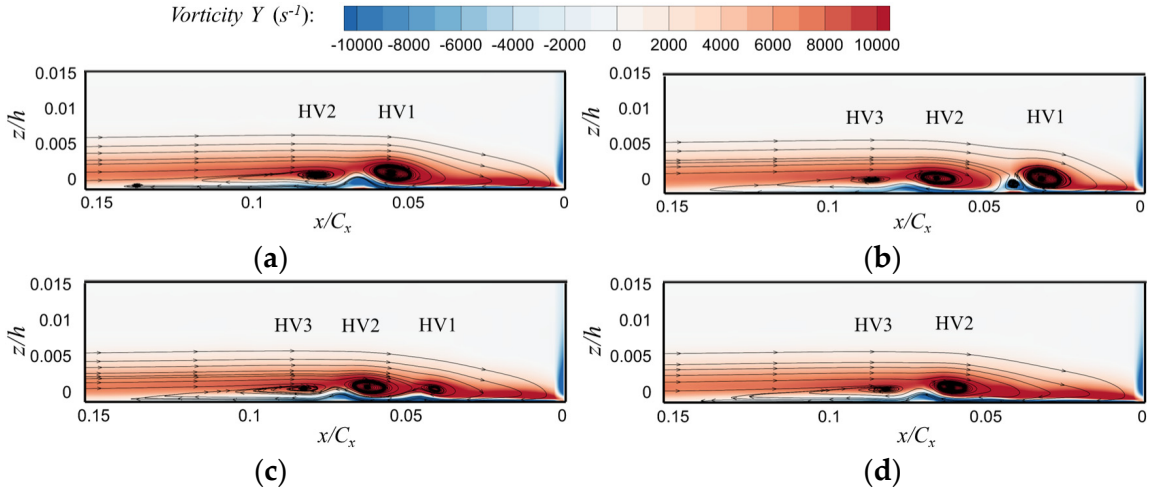

Figure 12. Typical flow pattern and circumferential vorticity contour of the HSV system in thin boundary layer conditions. (**a**) t = $1/4T_2^*$; (**b**) t = $2/4T_2^*$; (**c**) t = $3/4T_2^*$; (**d**) t = $4/4T_2^*$.

3.2.2. Analysis of Bimodal Dynamics of the HSV Vortex System

Figure 13 shows the bimodal dynamic probability density function diagram generated by HSV vortex system control at the position of Point 1 (shown in Figure 8) in two working conditions. Its horizontal axis is dimensionless and uses the root mean square value of the instantaneous flow disturbance velocity and flow disturbance velocity. Paik J. et al. [16] pointed out that (1) if the flow direction disturbance velocity in the influence range of the leading edge HSV vortex system presents a bimodal probability density function distributions, it indicates that the region is affected by two typical flow modes. (2) The peak value of the negative velocity component represents the back-flow mode of the near-wall reflux in a stable state, while the peak value of the positive velocity component represents the zero-flow mode of the reflux stability and vortex system alternation. (3) The velocity

component of the leading-edge HSV vortex system obeys a bimodal Gaussian distribution within the influence blade height range and a standard normal distribution outside the influence blade height range. In Figure 13, the flow field at multiple blade heights under two working conditions follows the probability density function distribution of the sum of two Gaussian functions. The probability density function is as follows:

$$f(x) = A\frac{1}{\sqrt{2\pi}\sigma_1}\exp\left(\frac{(x-\mu_1)^2}{2{\sigma_1}^2}\right) + B\frac{1}{\sqrt{2\pi}\sigma_2}\exp\left(\frac{(x-\mu_2)^2}{2{\sigma_2}^2}\right) \quad (8)$$

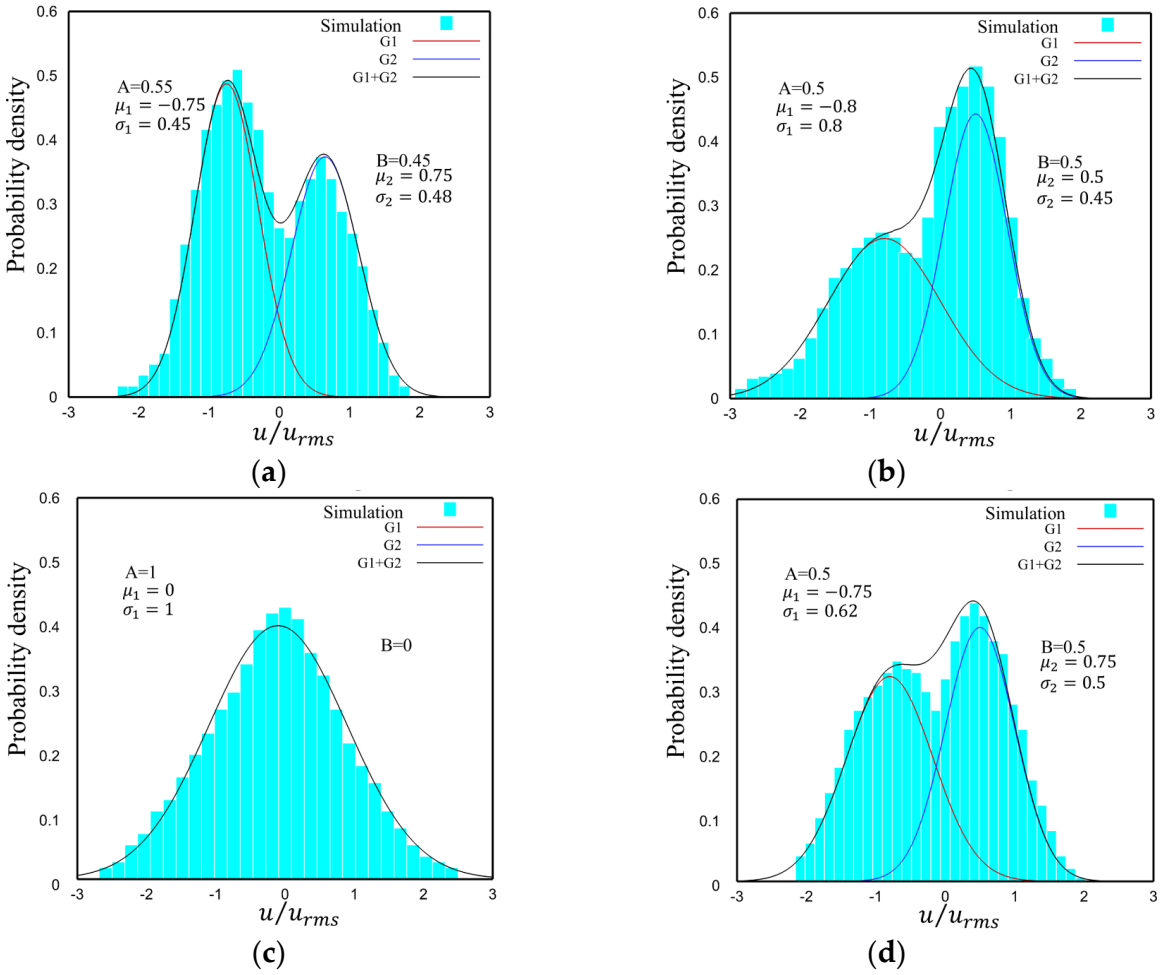

Figure 13. Point 1 probability density function diagram of the flow velocity component distribution at each height of the flow direction position. (**a**) Thick boundary layer case 0.2% blade height; (**b**) Thick boundary layer case 20% blade height. (**c**) Thick boundary layer case 40% blade height. (**d**) Thin boundary layer case 0.2% blade height.

A and $B \in [0, 1]$ and $A + B = 1$. A and B can be used to describe the percentage of the total calculation time for the mode; σ can represent the flow diversity or uncertainty of the flow field under the position. By comparing Figure 13a,d, it is found that μ at the same position with the same leaf height is very similar, indicating that it is affected by almost the same flow mode. The coefficient B of G2 in Figure 13d is larger than that in Figure 13a, which means that the zero-flow mode duration and the occupied energy are larger in the thin boundary layer case than in the thick boundary layer case. Moreover, the variance of both Gaussian distributions in Figure 13d is larger than that in Figure 13a. This shows that the two typical flow mode alternations are more frequent in the thin boundary layer case than in the thick boundary layer case during the full cycle.

3.2.3. POD Analysis of the Leading Edge HSV Vortex System

The POD method analyzes the characteristics of the dominant mode in the separation flow as a low-dimensional dynamic display technology for studying coherent structural dynamics and complex structural dynamic phenomena in turbulence. In this study, one of the statistical results was selected every ten times for analysis, and POD analysis was performed on the flow field disturbance velocity data of 500 Plane A, among which one HSV quasi-periodic cycle contained approximately 50-time steps. The POD analysis method used in this study is based on reference [43].

The energy share of each order mode of POD at Plane A is shown in Figure 14, where the vertical axis represents the proportion of energy of the mode flow field in the original flow field and the horizontal axis indicates the different modes. In the thick boundary layer case in Figure 14, the first six modes occupy 65% of the energy of the whole flow field, while the first four modes in the thin boundary layer case occupy more than 75% of the energy of the whole flow field. Thus, the abovementioned modes of the two cases are selected for analysis. In Figure 14, the energy of the thin boundary layer condition decays significantly faster than that of the thick boundary layer condition as the number of modes increases. This means that fewer modes occupy higher energy in the thin boundary layer condition, i.e., the thick boundary layer has a higher flow diversity and more flow patterns compared with the thin boundary layer.

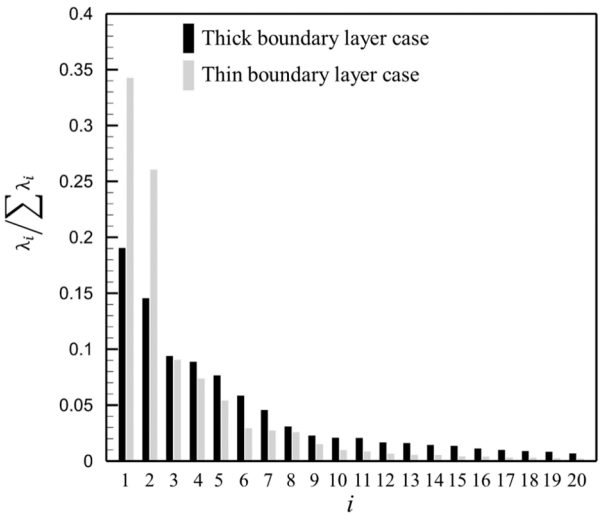

Figure 14. Energy distribution of POD modes.

Figure 15 shows the velocity vector and energy distribution in the first six modes of the POD flow field under thick boundary layer conditions. In Figure 15, the velocity vectors in the first six modes with the highest POD energy can correspond to the structural changes of the six typical flow vortex systems shown in Figure 11. Additionally, the positions of the high energy area coincide with the near-wall reflux and secondary flow vortex systems shown in Figure 11. The Mode 1 flow field corresponds to the flow state in Figure 11a, the Mode 2 flow field corresponds to the process flow state between Figure 11a,b, and Modes 4 and 3 correspond to the flow states of near-wall backflow in different degrees of outburst instability process in Figure 11b. Mode 5 corresponds to the flow state when the vortex system is fused to form a large-size vortex structure in Figure 11d. Mode 6 corresponds to the flow state in Figure 11e, in which the flow state occurs when the large-size vortex structure forms and begins to separate. This implies that the six typical modes in Figure 11 occupy the majority of the energy in the flow field. The modes that contain the most energy in the calculation results of the thick boundary layer condition are Mode 1, which occupies 19% of the energy, and Modes 2, 3, and 4, which occupy 33% of the total energy. The abovementioned three modes correspond to the flow state in which instability occurs due to the outbreak of reflux near the wall and the zero-flow mode.

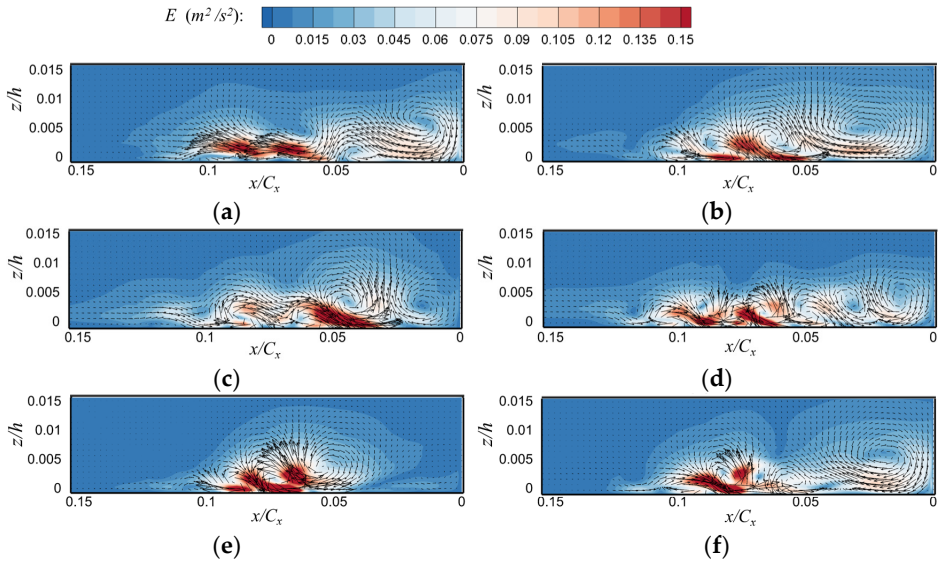

Figure 15. POD mode flow field in the thick boundary layer condition. (**a**) Mode 1 (**b**) Mode 2 (**c**) Mode 4 (**d**) Mode 3 (**e**) Mode 5 (**f**) Mode 6.

Figure 16 shows the mode flow field of the POD calculation results for the thin boundary layer condition. Modes 1 and 2 flow fields correspond to the flow states in Figure 12a,b, where near-wall reflux is in the process of eruption. Mode 4 corresponds to the flow state in Figure 12b, i.e., the zero flow mode, when the third vortex is successfully induced. Mode 3 corresponds to the flow state in Figure 12c, when HV1 and HV2 begin to fuse. In the thin boundary layer condition, Modes 1, 2, and 3 occupy 37%, 26.5%, and 7.5% of the total energy, respectively. The abovementioned three modes are related to the near-wall reflux eruption instability and the zero-flow mode, which occupy a total of 72% of the total energy in the flow field. This is much larger than the energy share of the first three modes in the thick boundary layer condition, which shows that the instability of near-wall reflux eruption occurs more frequently and for a longer period of time in the thin boundary layer conditions. This conclusion is consistent with the conclusions obtained from the HSV bimodal dynamics analysis.

The power spectral densities of the eigenvectors of each order of the POD modes are shown in Figure 17, and different modes have different dominant frequencies. According to the description by Paik [16], the dominant frequency of each order mode is the characteristic frequency of the near-wall surface reflux state under the flow field of that mode. Thus, the dominant frequency of each order mode can characterize the stability of near-wall surface reflux. The dominant frequencies of the first four order modes in Figure 17 can be matched with the near-wall surface reflux stability and instability phenomena in Figure 11. Modes 2, 3, and 4 contain more energy in the bottom wall reflux, which indicates that they are stimulated to produce the instability mechanism. Therefore, the dominant frequency of 125 Hz represents the near-wall reflux instability frequency. For the thin boundary layer condition, the POD calculation results also capture the dominant frequencies of near-wall reflux stability and instability, where the near-wall reflux in Modes 1, 2, and 4 flow fields is in the state of instability. Therefore, its dominant frequency is the main frequency of near-wall reflux stimulation, i.e., 175 Hz, while the near-wall reflux in the Mode 3 flow field is more stable, and its dominant frequency is the back-flow mode frequency of 125 Hz.

In the stability-related dominant frequency of near-wall reflux, the reflux instability frequency is 175 Hz for the thin boundary layer case and 125 Hz for the thick boundary layer case. The ratio of the two is 1.4, which is the same as the ratio of the two boundary layer thicknesses, according to the two-dimensional flat plate boundary layer outburst time period described by Agui [25] as follows:

$$T_B U_0 / \delta = k \tag{9}$$

where T_B is the boundary layer outbreak instability period, U_0 is the mainstream velocity, and δ is the boundary layer thickness.

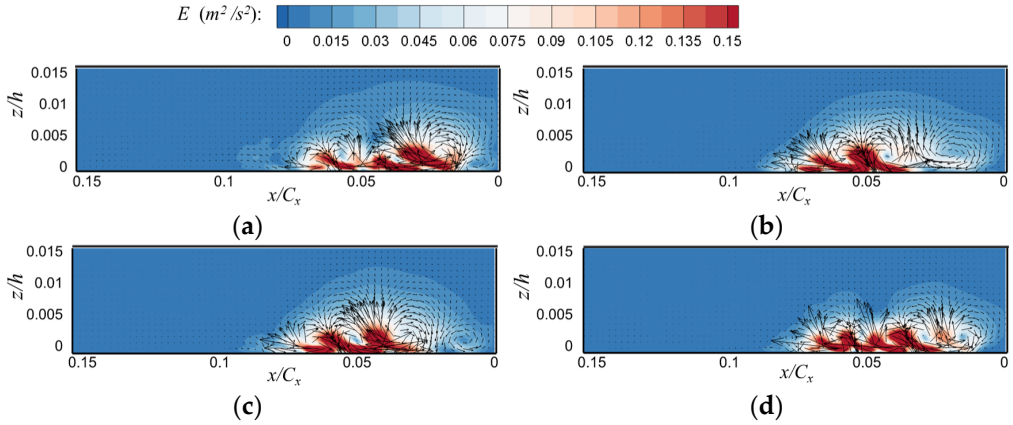

Figure 16. POD mode flow field in the thin boundary layer condition. (**a**) Mode 1 (**b**) Mode 2 (**c**) Mode 4 (**d**) Mode 3.

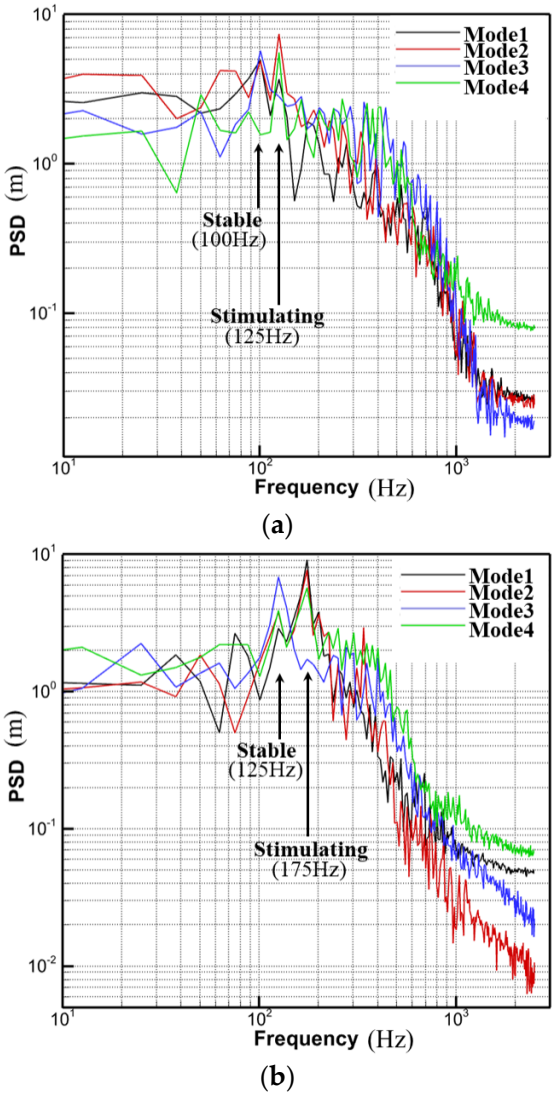

Figure 17. Mode flow spectrum at Plane A. (**a**) Thick boundary layer case (**b**) Thin boundary layer case.

Agui [25] suggested that the centrifugal instability of the HSV, which is caused by the interaction between the HSV and the wall, was the cause of the wall reflux outburst phenomenon. As shown in Figure 18a, we show the radial distribution of the velocity vector, the small velocity near the wall due to the viscous effect of the wall below the vortex system will cause an inflection point in the velocity distribution in the wall region of the vortex system (marked using the black dashed circle). Furthermore, according to the stability criterion proposed by Floryan [44], the boundary layer developed along the curved wall will have the potential for centrifugal instability when the velocity magnitude decreases with increasing radius of curvature, i.e., satisfying the inviscid criterion of Lord Rayleigh [45]:

$$\Phi(r) = \partial(ru_\theta)/\partial r < 0 \tag{10}$$

where r is the distance radius measured from the vortex nucleus, and the rotational velocity u_θ is the velocity component of the flow direction. The $\Phi(r)$ distribution curves for the two incoming boundary layer thickness conditions studied in this study are shown in Figure 18b. The radius range of $\Phi(r) < 0$ in the thin boundary layer condition is higher than that in the thick boundary layer condition. Due to the smaller size of the vortex system in the spanwise height, the thin boundary layer is closer to the wall. This is because the wall viscosity is higher, which meets Floryan's stability criterion in the larger vortex reflux range, while the near-wall reflux is less stable and more likely to cause reflux outbreaks. For the thick boundary layer case, this means that near-wall reflux happens less often in Figure 17b than it does in Figure 17a.

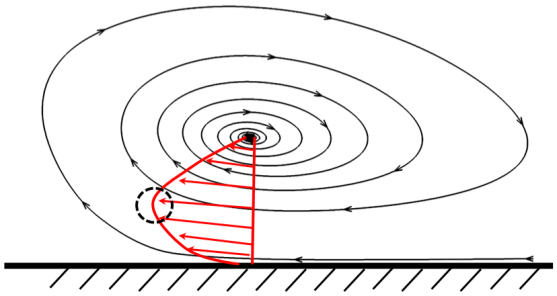

(**a**)

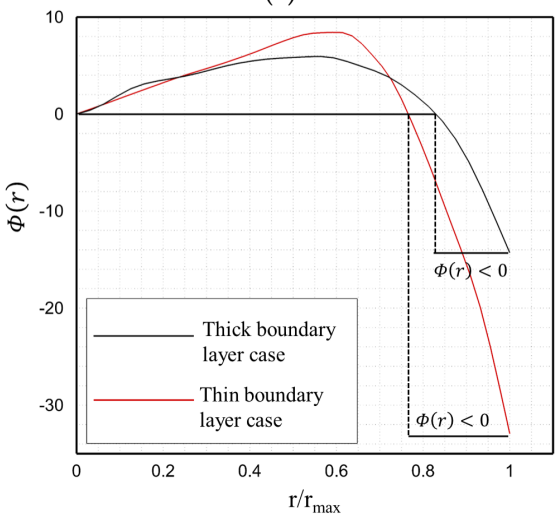

(**b**)

Figure 18. Centrifugal instability principle and instability characteristics under different boundary layer thicknesses. (**a**) Schematic diagram of the centrifugal instability principle (**b**) Lord Rayleigh's criterion for different boundary layer thicknesses.

3.2.4. Influence of the Unsteady Leading-Edge HSV Vortex System on the Secondary Flow in the Cascade Channel

Secondary kinetic energy is a quantity that can measure the intensity of secondary flow in the leaf grid channel. The secondary kinetic energy in the endwall is mainly composed of the kinetic energy of the secondary flow components in the Y-Z plane, which is defined as follows:

$$SKE = 1/2({v_{SEC}}^2 + {w_{SEC}}^2) \quad (11)$$

where v_{SEC} and w_{SEC} represent the secondary flow velocity components in the Y and Z directions, respectively. Since the horseshoe vortex in the passage is a vortex tube formed by the stretching of the HSV vortex system at the leading edge, the configuration of the horseshoe vortex in the cascade channel at different times is also different. By transforming the calculated results from the Eulerian method to the Lagrange method, the spatial locations of the fluid microclusters representing the flow patterns of vortex tubes in different HSV vortex systems can be obtained.

Figure 19 shows the calculation results of this method in the thick boundary layer condition, where SL and PL represent the fluid micromass track lines forming the suction and pressure surface branches of HSV, respectively. The time in Figure 19a–d is the initial moment when the fluid microclusters begin to move from the leading edge of the cascade. The instantaneous secondary flow energy amplitude when fluid microclusters move to different sections is shown in section cloud Figure 19 in the cascade channel. In the figure, a section is selected every $0.25C_x$. The secondary kinetic energy at different sections is a time variable that can represent the instantaneous secondary flow intensity at this position. The enlarged contour image at the top shows the flow pattern at the leading edge under the initial time-cut flow pattern selected by the Lagrange transform. Figure 19a corresponds to the back-flow mode in Figure 11a, the zero-flow mode in Figure 11b, the flow state in which the vortex system begins to fuse in Figure 11c, and the flow state in which the vortex system merges to form a large vortex in Figure 19d. Among them, the SKE represented by the contour image in Figure 19b was significantly higher than that in Figure 19a,c,d. In the amplified flow field of Figure 19b, the near-wall reflux is in a state of outburst instability. Therefore, compared with the amplified flow field of Figure 19a,c,d, its HSV vortex system is more unstable, thus enhancing the secondary flow of the endwall.

To more intuitively represent the influence of different initial flow modes on downstream secondary flow energy, Figure 19e shows the average statistical value of the SKE mass of four flow states and four flow directions in Figure 19a–d after processing. It is performed for the SKE value of the section, and it can be seen that under each initial flow state, the variation law along the flow position is the same. In the corresponding flow modes in Figure 19b, when the reflux of the leading edge endwall of the cascade is unstable, the HSV vortex system will increase the secondary flow intensity of the downstream endwall as the fluid microclusters develop downstream. This means that the SKE intensity of the vortex system at four moments in Figure 19b is higher than the other three initial flow modes. The intensity of SKE in Figure 19c,d is very similar and larger than that in Figure 19a. This occurs because the initial flow field of the cascade front shown in Figure 19c,d is a flow state in the process of vortex system alternation, which is highly unstable, while the initial flow field of the cascade front shown in Figure 19a is a stable flow state.

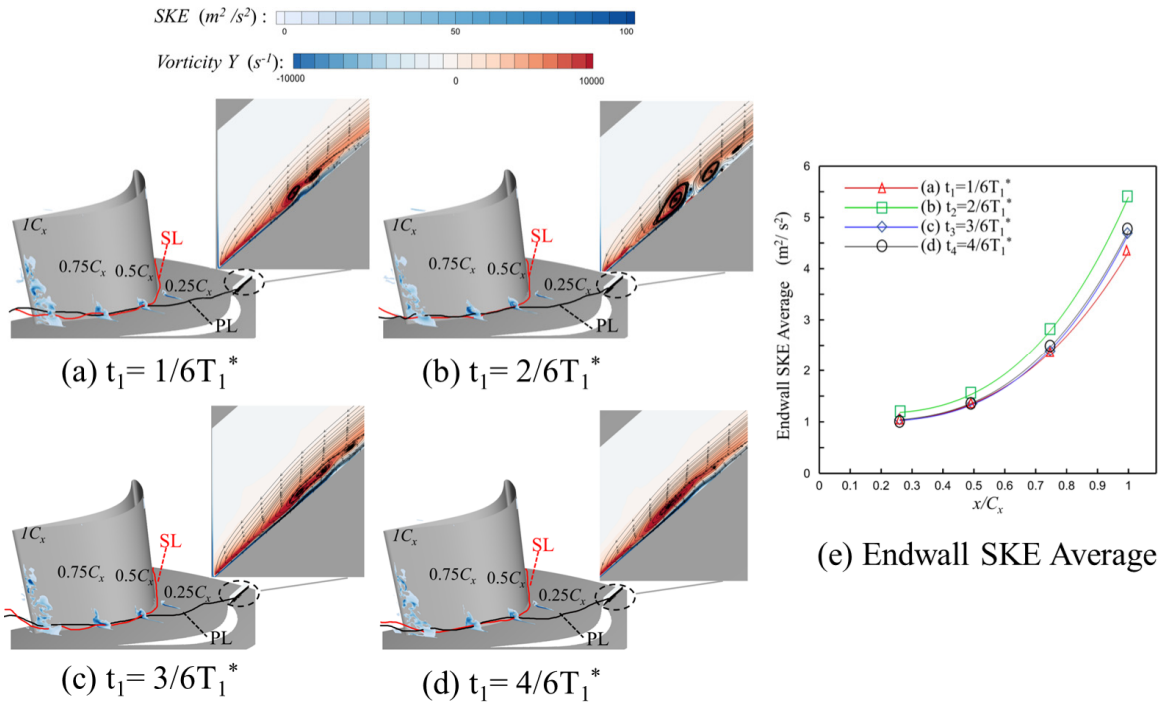

Figure 19. Secondary kinetic energy in cascade passage under different initial times of flow regime.

3.2.5. Effect of Different Boundary Layer Thicknesses on the Loss in the Cascade Channel

The time-averaged entropy generation characterizes the viscous losses of the time-averaged flow field in the non-pressurizable flow, which does not take into account the entropy gain from velocity fluctuations, i.e., it does not include the losses due to unsteady effects. Figure 20 shows the Q-criterion isogram within the cascade channel, colored using the fluctuating entropy generation [46]. In Figure 20a, the initial secondary flow intensity is higher compared to Figure 20 due to its larger vortex size and higher intensity, which in turn causes greater unsteady losses in the first half of the cascade channel. However, the vortex system is relatively stable, and the vortex fluctuation is weak. As the flow progresses downstream, the unsteady effect of Figure 20 gradually accumulates, and the unsteady loss in the channel gradually exceeds that of Figure 20. The difference between the time-averaged entropy generation of the two conditions is small, the thick boundary layer condition is slightly larger than the thin boundary layer condition, and the two conditions have large differences in fluctuating entropy generation.

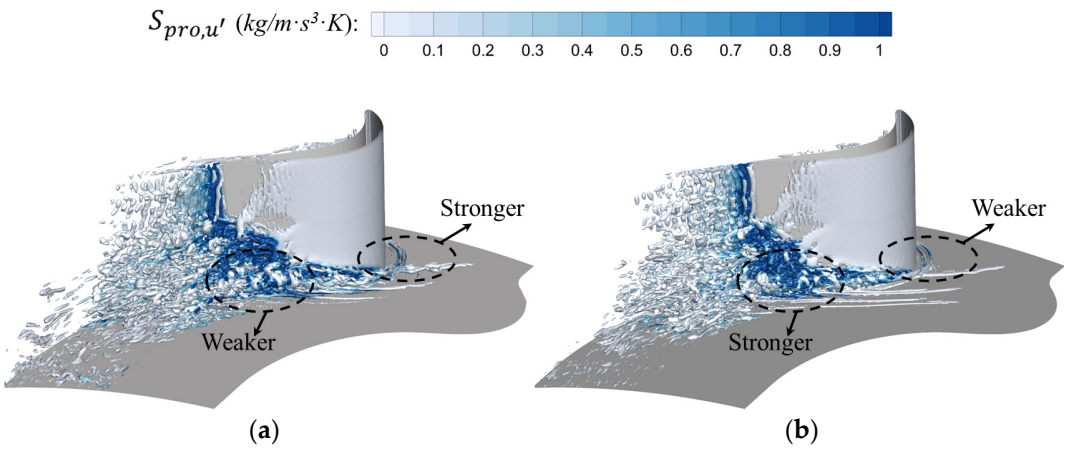

Figure 20. Structure of cascade channel vortex system and its fluctuating entropy generation distribution. (**a**) Thick boundary layer case (**b**) Thin boundary layer case.

Figure 21 shows the fluctuating entropy generation for the same four axial cross sections as Figure 19 is used to investigate the characteristics of the unsteady losses at different blade height positions within the cascade channel. In Figure 21, upstream of 50% C_x, the vortex size is larger and the secondary flow intensity is higher, which causes higher unsteady losses. Downstream of 50% C_x, the unsteady effect of Figure 21 gradually accumulates with the gradual development of the flow, and the unsteady loss caused by it is comparable to that in Figure 21. Since the fluctuating production of entropy is very different between the two working conditions, this shows that the mechanism of unsteady loss is different for each.

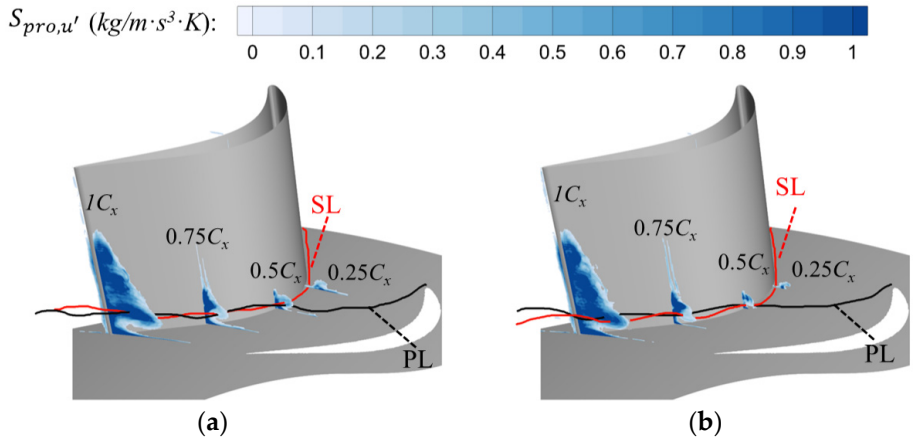

Figure 21. Fluctuating entropy generation distribution of the flow section in the turbine cascade channel. (**a**) Thick boundary layer case (**b**) Thin boundary layer case.

3.3. Analysis of the Unsteady Characteristics of the Cascade Outlet

The energy proportion of POD modes at $0.2C_x$ downstream of the cascade channel is shown in Figure 22 Compared with the mode flow field at the leading edge (Figure 15, the mode flow field energy at the trailing edge decays slowly with the number of modes, and the energy proportion of all modes except Mode 1 is roughly the same. The results show that, except for the vortex structure of the Mode 1 flow field, the strength of relevant vortex system structures in other modes is about the same in both working conditions. The vortex system structures mainly affected by different boundary layer thicknesses are those captured in the flow field of Mode 1, while the vortex system structures captured by Mode 2 and later modes have almost no influence.

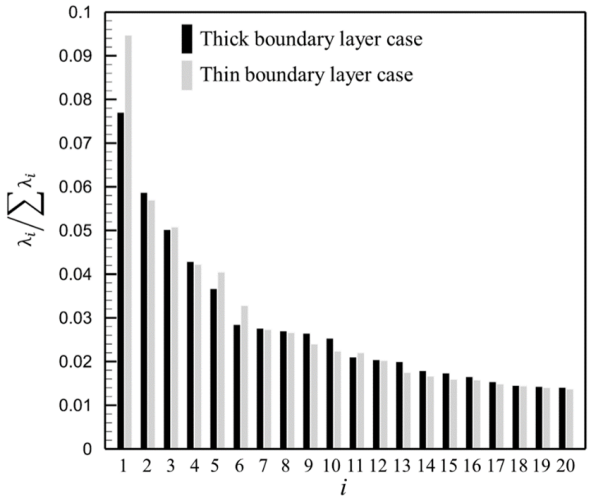

Figure 22. POD mode energy distribution at $0.2C_x$ downstream of the cascade.

Figure 23 shows the POD results of the first five modes occupying higher energy at $0.2C_x$ downstream of the cascade channel for both conditions. The contour is the energy in the POD mode flow field, and the perturbation velocity vector in the mode flow field is superimposed on the contour. The abovementioned POD results can determine the different vortex structures captured. In both conditions, the Mode 1 flow field mainly captures the passage vortex, the Mode 2 flow field mainly captures the wall vortex, and the Modes 3–5 flow field mainly has three vortices at the same time. Comparing the vortex structure and energy distribution of the POD mode flow field in the two conditions, it can be seen that the energy share of the Mode 1 flow field corresponding to Figure 23a is smaller than that in Figure 23b. This means that the thin boundary layer case in Figure 23b is more likely to induce the vortex instability alternation phenomenon due to the poor stability of the vortex system. Therefore, its stimulation of the channel vortex is stronger, and thus, the energy share of the passage vortex in the downstream flow field is higher. At the same time, the unsteady characteristics of the leading-edge vortex system and vortex system alternation do not affect the wall vortex, trailing-edge shedding vortex, and other vortex systems, indicating that the main target of the unsteady characteristics is the passage vortex.

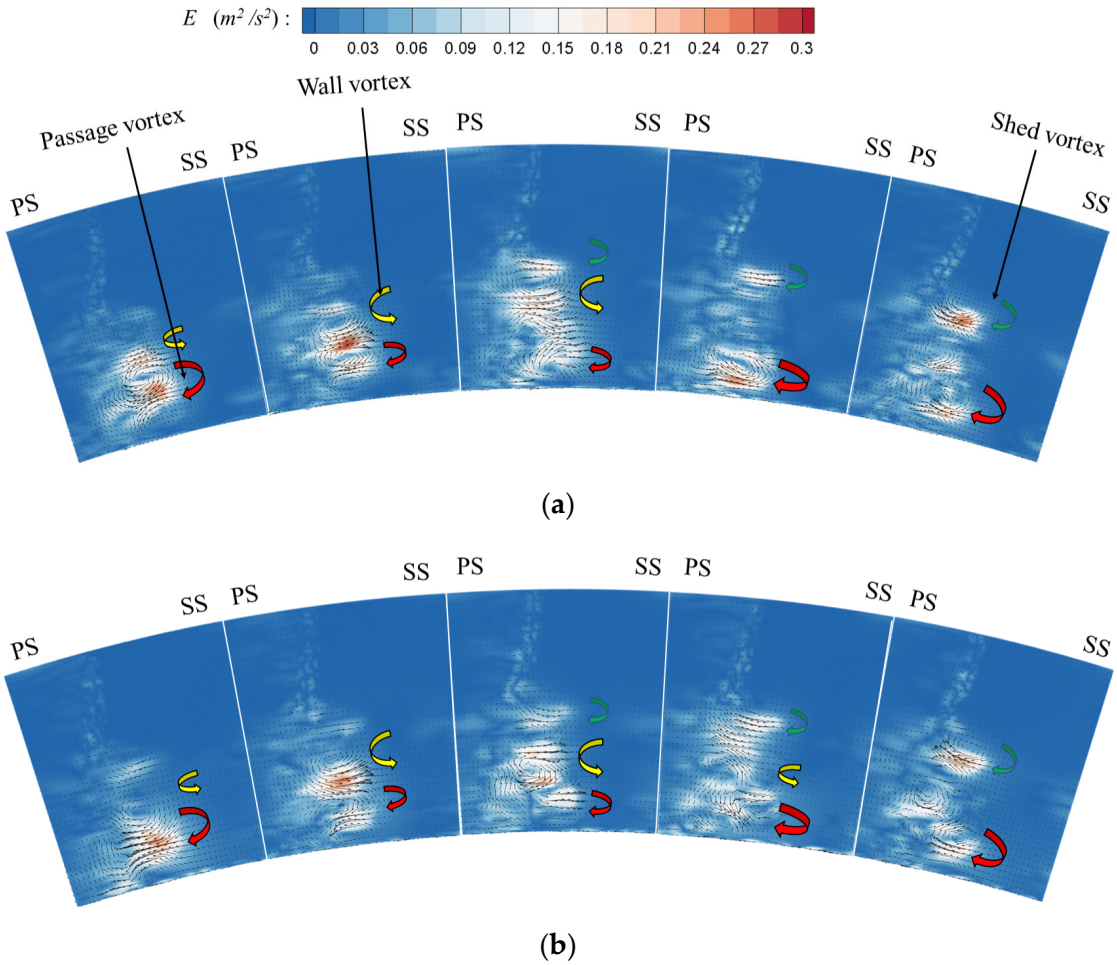

Figure 23. POD mode at $0.2C_x$ downstream of the cascade. (**a**) Thick boundary layer case (**b**) Thin boundary layer case.

4. Conclusions

In this study, the unsteady characteristics of HSV with two incoming flow boundary layer thicknesses are comprehensively studied. The time-averaged flow field and transient flow field of the two conditions are analyzed separately, and the main conclusions are as follows:

(1). We use the Smagorinsky model to calculate transient flow and use the Van-Driest wall dumping function to modify the model. Although this method cannot completely eliminate the disadvantages of the Smagorinsky model, it can still capture the configuration changes of leading-edge vortex systems. Compared with the RANS method, it has a better transient flow-capturing effect. Therefore, these results can be interpreted as possible, stable solutions.

(2). Under different boundary layer thickness conditions, there are abundant leading edge flow states, and they change in different ways. At the same Reynolds number, the thick boundary layer case has more diverse and stable vortex systems, while the thin boundary layer case has fewer fundamental flow states, but its vortex system alternates more frequently.

(3). The frequency of instability of reflux at a certain Reynolds number is inversely proportional to the boundary layer thickness. The instability is caused by centrifugal instability, which has different frequencies in different boundary layer thickness conditions due to the different percentages of its instability region. Different flow patterns in the leading edge of the cascade have different influences on the downstream. When the hub endwall reflux in the flow field is in an unstable state, its contribution to the downstream SKE is greater than that in the stable state. The contribution of each flow state in the unstable state to the secondary flow intensity is also different, but the difference is small.

(4). Different boundary layer thicknesses will have different effects on the loss in the channel, especially the unsteady fluctuation loss. The horseshoe vortex intensity in the thick boundary layer case is higher than that in the thin boundary layer case due to the larger vortex size. As a result, the unsteady fluctuation loss in front of the cascade channel is greater than that in the thin boundary layer case, and the stability of the vortex system is different between the two. With the gradual accumulation of unsteady fluctuations, the unsteady fluctuation loss caused by the thin boundary layer case gradually exceeds that of the thick boundary layer case.

(5). The change in the flow pattern at the leading edge affects the change in the strength of the passage vortex. The leading edge reflux is frequently destabilized, increasing the passage vortex intensity, whereas it does not affect the wall vortex and shedding vortex.

Author Contributions: Conceptualization, J.K. and Z.H.; methodology, J.K.; software, Z.H.; validation, Z.L., X.W. and H.S.; formal analysis, J.K.; investigation, H.S.; resources, S.S.; data curation, X.W.; writing—original draft preparation, J.K.; writing—review and editing, S.S.; visualization, S.S.; supervision, Z.L.; project administration, S.S.; funding acquisition, S.S. All authors have read and agreed to the published version of the manuscript.

Funding: Science Center for Gas Turbine Project (P2022-B-II-008-001, P2022-DC-II-001-001).

Data Availability Statement: Due to privacy restrictions, we cannot share our research data.

Acknowledgments: Thanks are given for the support of the Science Center for Gas Turbine Project (P2022-B-II-008-001, P2022-DC-II-001-001).

Conflicts of Interest: The authors declare no conflict of interest.

References

1. Ito, E.; Tsukagoshi, K.; Masada, J.; Ishizaka, K.; Saitoh, K.; Torigoe, T. Key Technologies for Ultra High Temperature Gas Turbines. *Mitsubishi Heavy Ind. Tech. Rev.* **2015**, *52*, 15–23.
2. Chen, L.D.; Dixon, S.L. Growth of Secondary Flow Losses Downstream of a Turbine Blade Cascade. *J. Aerosp. Power* **1986**, *108*, 270–276. [CrossRef]
3. Gregory-Smith, D.G.; Graves, C.P.; Walsh, J.A. Growth of Secondary Losses and Vorticity in an Axial Turbine Cascade. *J. Turbomach.* **1988**, *110*, 1. [CrossRef]
4. Harrison, S. Secondary Loss Generation in a Linear Cascade of High-Turning Turbine Blades. *J. Turbomach.* **1990**, *112*, 618–624. [CrossRef]

5. Macisaac, G.D.; Sjolander, S.A.; Praisner, T.J. Measurements of Losses and Reynolds Stresses in the Secondary Flow Downstream of a Low-Speed Linear Turbine Cascade. In Proceedings of the ASME Turbo Expo 2010: Power for Land, Sea, and Air, Glasgow, UK, 14–18 June 2010.
6. Satta, F.; Simoni, D.; Ubaldi, M.; Zunino, P.; Bertini, F. Profile and Secondary Flow Losses in a High-Lift LPT Blade Cascade at Different Reynolds Numbers under Steady and Unsteady Inflow Conditions. *J. Therm. Sci.* **2012**, *21*, 483–491. [CrossRef]
7. Dossena, V.; Ippolito, G.D.; Pesatori, E. Stagger Angle and Pitch-Chord Ratio Effects on Secondary Flows Downstream of a Turbine Cascade at Several Off-Design Conditions. In Proceedings of the ASME Turbo Expo 2004, Vienna, Austria, 14–17 June 2004; GT2004-54083.
8. Weiss, A.P.; Fottner, L. The Influence of Load Distribution on Secondary Flow in Straight Turbine Cascades. *J. Turbomach.* **1995**, *117*, 133–141. [CrossRef]
9. Langston, L.S. Crossflows in a Turbine Cascade Passage. *J. Eng. Gas Turbines Power* **1980**, *102*, 866–874. [CrossRef]
10. Hodson, H.P.; Dominy, R.G. Three-Dimensional Flow in a Low Pressure Turbine Cascade at Its Design Condition. *J. Turbomach.* **1987**, *109*, 177–185. [CrossRef]
11. Zoric, T.; Popovic, I.; Sjolander, S.A.; Praisner, T.; Grover, E. Comparative Investigation of Three Highly Loaded LP Turbine Airfoils: Part I—Measured Profile and Secondary Losses at Design Incidence. In Proceedings of the ASME Turbo Expo 2007, Montreal, QC, Canada, 14–17 May 2007. GT2007-27537.
12. Zoric, T.; Popovic, I.; Sjolander, S.A.; Praisner, T.; Grover, E. Comparative Investigation of Three Highly Loaded LP Turbine Airfoils: Part II—Measured Profile and Secondary Losses at Off-Design Incidence. In Proceedings of the ASME Turbo Expo 2007, Montreal, QC, Canada, 14–17 May 2007. GT2007-27538.
13. Torre, D.; Vázquez, R.; de la Rosa Blanco, E.; Hodson, H.P. A New Alternative for Reduction in Secondary Flows in Low Pressure Turbines. *J. Turbomach.* **2011**, *133*, 011029. [CrossRef]
14. Praisner, T.J.; Smith, C.R. The Dynamics of the Horseshoe Vortex and Associated Endwall Heat Transfer—Part I: Temporal Behavior. *J. Turbomach.* **2005**, *128*, 747–754. [CrossRef]
15. Devenport, W.J.; Simpson, R.L. Time-dependent and time-averaged turbulence structure near the nose of a wing-body junction. *J. Fluid Mech.* **1990**, *210*, 23–55. [CrossRef]
16. Paik, J.; Escauriaza, C.; Sotiropoulos, F. On the bimodal dynamics of the turbulent horseshoe vortex system in a wing-body junction. *Phys. Fluids* **2007**, *19*, 23–27. [CrossRef]
17. Escauriaza, C.; Sotiropoulos, F. Reynolds Number Effects on the Coherent Dynamics of the Turbulent Horseshoe Vortex System. *Flow Turbul. Combust.* **2011**, *86*, 231–262. [CrossRef]
18. Apsilidis, N.; Diplas, P.; Dancey, C.L.; Bouratsis, P. Time-resolved flow dynamics and Reynolds number effects at a wall-cylinder junction. *J. Fluid Mech.* **2015**, *776*, 475–511. [CrossRef]
19. Chen, Q.; Qi, M.; Zhong, Q.; Li, D. Experimental study on the multimodal dynamics of the turbulent horseshoe vortex system around a circular cylinder. *Phys. Fluids* **2017**, *29*, 015106. [CrossRef]
20. Chrisohoides, A.; Sotiropoulos, F.; Sturm, T.W. Coherent structures in flat-bed abutment flow: Computational fluid dynamics simulations and experiments. *J. Hydraul. Eng.* **2003**, *129*, 177–186. [CrossRef]
21. Hussein, H.J.; Martinuzzi, R.J. Energy balance for turbulent flow around a surface mounted cube placed in a channel. *Phys. Fluids* **1996**, *8*, 764–780. [CrossRef]
22. Kalitzin, G.; Medic, G.; Iaccarino, G.; Durbin, P. Near-wall behavior of RANS turbulence models and implications for wall functions. *J. Comput. Phys.* **2005**, *204*, 265–291. [CrossRef]
23. Dargahi, B. The turbulent flow field around a circular cylinder. *Exp. Fluids* **1989**, *8*, 1–12. [CrossRef]
24. Simpson, R.L. Junction Flows. *Annu. Rev. Fluid Mech.* **2001**, *33*, 415–443. [CrossRef]
25. Agui, J.H.; Andreopoulos, J. Experimental investigation of a three-dimensional boundary layer flow in the vicinity of an upright wall mounted cylinder. *Trans. ASME* **1992**, *114*, 566–576.
26. Shah, K.B.; Ferziger, J.H. A fluid mechanicians view of wind engineering: Large eddy simulation of flow past a cubic obstacle. *J. Wind Eng. Ind. Aerodyn.* **1997**, *67*, 211–224. [CrossRef]
27. Krajnovic, S.; Davidson, L. Large eddy simulation of the flow around a three-dimensional bluff body. In Proceedings of the 39th Aerospace Sciences Meeting and Exhibit, Reno, NV, USA, 8–11 January 2001.
28. Su, X.; Bian, X.; Li, H.; Yuan, X. Unsteady flows of a highly loaded turbine blade with flat endwall and contoured endwall. *Aerosp. Sci. Technol.* **2021**, *118*, 106989. [CrossRef]
29. Bear, P.; Wolff, M.; Gross, A.; Marks, C.R.; Sondergaard, R. Experimental Investigation of Total Pressure Loss Development in a Highly Loaded Low Pressure Turbine Cascade. In Proceedings of the ASME Turbo Expo 2017, Charlotte, NC, USA, 26–30 June 2017.
30. Gross, A.; Romero, S.; Marks, C.R.; Sondergaard, R. Numerical Investigation of Low-Pressure Turbine Endwall Flows. In Proceedings of the AIAA Scitech 2016, San Diego, CA, USA, 4–8 January 2016.
31. Tomikawa, K.; Horie, H.; Arakawa, C. Parametric surveys of the effects of wake passing on high lift LP turbine flows using LES. In Proceedings of the ASME/JSME 2007 5th Joint Fluids Engineering Conference, San Diego, CA, USA, 30 July–2 August 2007.
32. Funazaki, K.I.; Yamada, K.; Tanaka, N.; Chiba, Y. Detailed Studies on Separated Boundary Layers over Low-Pressure Turbine Airfoils under Several High Lift Conditions: Effect of Freesteam Turbulence. In Proceedings of the ASME Turbo Expo 2009: Power for Land, Sea and Air, Orlando, FL, USA, 8–12 June 2009; GT2009-59813.

33. Ooba, Y.; Kodama, H.; Arakawa, C.; Matsuo, Y. Numerical simulation of a Wake-Blade Interaction using LES. In Proceedings of the 17th Symposium on Computational Fluid Dynamics, Cambridge, UK, 11–14 July 2002.
34. Shi, W.; Ning, G.; Lin, C.; Tang, D. Numerical simulation and analysis of horseshoe-shaped vortex in near-wall region of turbulent boundary layer. *Trans. Nanjing Univ. Aeronaut. Astronaut.* **2011**, *28*, 48–56.
35. Sun, S.; Tan, T.; Wu, X.; Lu, X.; Zhang, Y.; Zhu, J. Influence of the Upstream Wakes on the Boundary Layer of a High-Lift Low-Pressure Turbine at Positive Incidence. *J. Aerosp. Eng.* **2020**, *33*, 04020077. [CrossRef]
36. Pope, S.B. *Turbulent Flows*; Cambridge University Press: Cambridge, MA, USA, 2000.
37. Deardorff, J.W. A numerical study of three-dimensional turbulent channel flow at large Reynolds numbers. *J. Fluid Mech.* **1970**, *41*, 453–480. [CrossRef]
38. Roach, P.E. The Generation of Nearly Isotropic Turbulence by Means of Grids. *Int. J. Heat Fulid Flow* **1987**, *8*, 82–92. [CrossRef]
39. Hinze, J.O. *Turbulence*, 2nd ed.; McGraw-Hill: New York, NY, USA, 1975.
40. Bich, W.; Cox, M.G.; Dybkaer, R.; Elster, C.; Estler, W.T.; Hibbert, B.; Imai, H.; Kool, W.; Michotte, C.; Nielsen, L.; et al. Revision of the 'Guide to the Expression of Uncertainty in Measurement'. Why and how. *Metrologia* **2014**, *51*, S155. [CrossRef]
41. Mahallati, A.; McAuliffe, B.R.; Sjolander, S.A.; Praisner, T.J. Aerodynamics of a low-pressure turbine airfoil at low reynolds numbers—Part I: Steady flow measurements. *J. Turbomach.* **2013**, *135*, 011010. [CrossRef]
42. Baker, C.J. The turbulent horseshoe vortex. *J. Wind Eng. Ind. Aerodyn.* **1980**, *6*, 9–23. [CrossRef]
43. Sun, S.; Wu, X.; Huang, Z.; Hu, X.; Zhang, P.; Kong, Q. Experimental and numerical investigation of periodic downstream potential flow on the behavior of boundary layer of high-lift low-pressure turbine blade. *Aerosp. Sci. Technol.* **2022**, *123*, 107453. [CrossRef]
44. Floryan, J.M. Goertler instability of boundary layers over concave and convex walls. *Phys. Fluids* **1986**, *29*, 2380–2387. [CrossRef]
45. Rayleigh, L. On the Dynamics of Revolving Fluids. *Proc. R. Soc. Lond.* **1917**, *93*, 148–154. [CrossRef]
46. Herwig, H.; Kock, F. Direct and indirect methods of calculating entropy generation rates in turbulent convective heat transfer problems. *Heat Mass Transf.* **2007**, *43*, 207–215. [CrossRef]